Final Draft
of the original manuscript:

Amancio, S.; Sheikhi, S.; dos Santos, J.; Bolfarini, C.:
Preliminary study on the microstructure and mechanical properties of dissimilar friction stir welds in aircraft aluminium alloys 2024-T351 and 6056-T4
In: Journal of Materials Processing Technology (2007) Elsevier

DOI: 10.1016/j.jmatprotec.2007.12.008

Preliminary Study on the Microstructure and Mechanical Properties of Dissimilar Friction Stir Welds in Aircraft Aluminium Alloys 2024-T351 and 6056-T4.

S.T. Amancio-Filho [a, c, *], S. Sheikhi [a], J.F. dos Santos [a], C. Bolfarini [b]

[a] *GKSS Forschungszentrum Geesthacht GmbH, Institute of Materials Research, Max-Planck-Str. 1, D-21502 Geesthacht, Germany.*

[b] *Federal University of São Carlos, Department of Materials Engineering, Rod. Washington Luiz km. 235, P.O.Box 676, 13565-905 São Carlos-SP, Brazil.*

[c] *CNPq-Brazil GDE-Ph.D. scholarship holder.*

[*] Corresponding author. Tel. +49 4152 87 2066; fax: +49 4152 87 2033. E-mail address: sergio.amancio@gkss.de (S.T. Amancio-Filho)

Abstract

Aircraft aluminium alloys generally present low weldability by traditional fusion welding process. The development of the friction stir welding has provided an alternative improved way of satisfactory producing aluminium joints, in a faster and reliable manner. In the present work dissimilar Al alloys (AA2024-T351 and AA6056-T4) were friction stir welded. Butt joints were obtained by varying process parameters, namely the rotational speed (500-1200 rpm) and the welding speed (150-400 mm/min.), while axial force and tool geometry were kept constant. Parameter optimisation, which has been based on the results of

macrographic analysis and microhardness testing, indicated that sound joints can be obtained in the parameters range of rotational speed equal to 800 rpm and welding speed of 150 mm/min. Light and scanning electron microscopy in several positions revealed the presence of a lamellar material flow pattern due to the differential flow, suggesting material mechanical mixing within the stirred zone. High level of strain and temperatures usually over 400 ^{o}C, resulted in a dynamically recrystallised stirred zone with refined grains. Tensile testing (standard flat L-T samples) has shown that strength is up to 90% of the weakest joining partner 6056-T4. Fracture took place in the thermo-mechanically heat affected zone of the alloy 6056-T4, where annealed structure led to decrease in microhardness. This behaviour was confirmed by microflat tensile testing, which indicated the drop in tensile strength and the associated increase of strain, in the regions of microhardness drop. This study has shown that in a dissimilar friction stir weld, the weaker component dictates the performance of the joint, where failure happens in the region of the greatest strength reduction related to annealing phenomena. Microscopic investigation as well as the evaluation of local mechanical properties has suggested that mechanical mixing is the major material flow mechanism in the formation of the stirred zone.

Keywords: aluminium; friction stir welding; aircraft; welding; dissimilar joints; microstructure.

1. Introduction

Friction Stir Welding (FSW), developed and patented by TWI, Cambridge [1] has demonstrated a significant potential for joining low melting point non-ferrous metals, especially difficult to weld aluminium alloys producing satisfactory mechanical properties [2]. A detailed description of the FSW process can be found in [3].

Aluminium alloys such as AA2024 and AA7075, which are widely used in aircraft structures, are usually associated with weldability problems [4]. Two precipitation hardenable aluminium alloys were selected for this study, the AA2024-T351 and the AA6056-T4. The AA2024-T351 alloy exhibits poor weldability by fusion processes but has been shown to be successfully welded by FSW [5, 6]. The major hardening particles in alloy AA2024 are Al_2Cu-θ formed by a complex precipitation process. The equilibrium phase θ has a thick platelike shape, with body-centred-hexagonal structure. The alloy AA6056-T4 is a variant of the AA6013 developed to replace the alloy AA2024-T3 in aircraft structures [7], based on Si-Mg-Zn-Cu-Mn additions in order to improve weldability, without loss of strength and corrosion properties [8], resulting in comparable mechanical properties to those observed in the AA2024 alloys [9]. Two main particles can be observed in the microstructure: a quaternary phase Q-$Al_5Cu_2Mg_8Si_6$-λ [10,11] and Mg_2Si-β [9]. The Q-phase shape is round or oval at grain boundaries [11] whilst the β-phase is plate shaped with a CFC structure [12].

There are a number of potential applications of the FSW process in aircraft structures, particularly in the case of dissimilar joints, whereby possible multi-material configurations involve among others the alloys AA2024, AA6056, AA6013 and AA7075. Concerning FSW of dissimilar precipitation-hardenable aluminium alloys, very little information is available in the literature. Murr et al [13], have investigated the system 2024/6061. A rotational speed range of 400-1200 rpm and a welding speed of 1 m/min were used. The authors [13] concluded that the alloy with lower hardness would be the limiting factor on performance. The microstructure exhibited by the dissimilar welds is comparable to those of similar welds, but with singular lamellae flow pattern of the base materials in the stir zone. This was interpreted as due to the differential viscosity of each alloy during welding [14]. Ying et al [15] have also studied the system 2024/6061 describing microstructural development and related mechanical properties of this joint.

The present study has been devised to extend the knowledge on metallurgy and performance of dissimilar FSW joints in precipitation-hardenable Al alloys involving a recently developed highly damage tolerant 6xxx series alloy and a consolidated commercial 2XXX alloy.

2. Materials and experimental procedure

4 mm thick plates of aluminium 2024-T351 (experimental chemical composition in Table 1) and 6056-T4 (experimental chemical composition in

Table 2) alloys were friction stir welded in a butt joint configuration. The alloy 2024-T351 was placed on the advancing side as recommend in the literature [16]. Larsson and Karlsson [17] employed a similar strategy when joining Al alloys 5XXX/6XXX by placing the stronger alloy on the advancing side.

A modular FSW tool with 5mm diameter threaded cylindrical pin and 15mm concave shoulder was employed (Fig. 1). All welds were performed using a TRICEPT TR805 robot equipped with an in-house developed and manufactured FSW unit operating in load and rotational speed control (Fig. 2). Further details on the robot and FSW unit can be found in [18, 19]. The tool rotational speed was varied from 500 to 1200 rpm and the welding speed from 150 to 400 mm/min.

In order to select appropriate process parameters for the testing programme a number of welds were produced. Macrographs of these joints were obtained transverse to the welding direction and observed in a light optical microscope. A double etching technique was used (Flick, 90 ml H_2O, 15 ml HCl 32%, 10 ml HF 40% to reveal 2024 and Dix-Keller, 190 ml H_2O, 5 ml HNO_3 65%, 3 ml HCl 32%, 2 ml HF 40% to reveal 6056) to reveal the stir zone. Vickers microhardness ($HV_{0,2}$) (ASTM E384-992e1 [20]) profiles of each weld were obtained using a Shimadzu HMV-200 with a load of 200 p (1,96 N). These measurements were performed at mid-thickness. Subsequently the joints were subjected to three point bending test (EN DIN 910 [21]).

Once optimised parameters have been selected from the results of micrographic analysis and microhardness testing in terms of the absence of defects and the reduced level of microhardness undermatching in the nugget area, a number of specimens have been produced for the actual test programme planned for this study. Three sections (Fig. 3) of the weld seam were analysed by optical and scanning electron microscopy. The mechanical properties of the joints were determined by testing conventional (L-T) flat tensile specimens (EN DIN 895 [22]) and microflat tensile specimens at room temperature [23]. Microflat tensile specimens were extracted across the joint as illustrated in Fig. 4.

Temperature measurements were obtained at the plate surface using an infrared camera and mid-thickness using the set of 30 cromel-alumel thermocouples. Figure 5 shows the equipment and the measuring system used in each case. For the infrared measurements an appropriate paint was applied to the surface of the plates (see Fig. 5(a)). Fifteen thermocouples were placed on each side of the weld (number 1 to 15 on AA6056 side and 16 to 30 on AA2024 side). The placement of thermocouples is illustrated in Fig. 5(b). A thermo-conductive paste was added to attach the thermocouples into the holes and to guarantee good contact to the surface.

3. Results and discussions

3.1. Determination of Optimised Weld Parameters

The parameters selected for this work (based on the results of preliminary investigations) were: welding speed of 150 mm/min and rotational speed of 800 rpm. More recent studies [24] have shown that by employing conical pin tools with five flats, higher welding speeds can be achieved. Moreover the mixing conditions provided by tools with flats also allow a more flexible placement of the alloys with respect to the welding and tool rotational direction.

3.2. Temperature Measurements

Figure 6(a) and (b) present the measured peak temperatures recorded by each of the thermocouples at the advancing and retreating side, respectively. Temperatures in the order of 350-400 ^{o}C were obtained for the two thermocouples nearest the weld centre (T.15 and T.30). Temperatures measured at the plate surface were comparable to those measured by the thermocouples, i.e. laying within the range 300-400 ^{o}C close to the weld centre.

3.3. Base Materials: Microstructure and Microhardness

Figure 7 presents the base material microstructure in the rolling direction. In Figure 7 (a) indicates the presence of elongated grains in the rolling direction of the AA2024-T351 alloy. SEM-BSE images in Fig. 7(b) show copper rich particles as verified in EDS analysis. These particles are second phase $\theta-CuAl_2$, typical of 2XXX alloys [25]. Fig. 7(c) presents the microstructure of the AA6056-T4 alloy also displaying grains oriented in the rolling direction. Fig. 7(d) presents a SEM-BSE image of this alloy, where two kinds of particles were observed: particles rich in Mg and Si, identified as the intermetallic β-Mg_2Si and particles rich in Mn and Fe, with compositions typical of secondary particles [11]. The measured average microhardness for AA2024-T351 was 144 $HV_{0,2}$ and for AA6050-T4 was 113 $HV_{0,2}$.

3.4. Welded Joint: Microstructure and Microhardness

Fig. 8 presents a schematic photo-montage of the weld macrostructure where the cross, longitudinal and xz sections are highlighted (see also Fig. 3).

A cross section of the friction stir weld (see Fig. 9(a)) reveals a well formed stir zone with a lamellar pattern formed by dark and bright lamellae as was also observed by Murr et al [13] for 2XXX/6XXX aluminium dissimilar joints. No internal defects have been observed (defect-free joints) in samples examined within different points of the weld seam from investigated joints. Fig.

9(b) shows the microhardness profiles for this section, which is divided in four typical microstructural regions [26]: base material (BM), heat affected zone (HAZ), thermo-mechanically affected zone (TMAZ) and stir zone. On the HAZ's (-20 to -10 mm and 5 to 15 mm, respectively) a decrease in microhardness is observed due to the accelerated ageing and recovering processes caused by the weld thermal cycle, as reported by Threadgill [26]. In these regions microhardness peaks can be observed, disrupting the declining trend of the microhardness profiles. This feature is discussed later on in the present work. On the TMAZ's (-10 to -5 mm and 2 to 5 mm, respectively) the microhardness minima for both alloys can be observed, explained by the local dissolution of strengthening particles and a reduction in the dislocation density. Nevertheless, closer to the transition between TMAZ and stir zone, an increase in microhardness was observed and this is thought to be due to a degree of work hardening (proximity to tool centre) [26]. On the stir zone, the increase in microhardness is associated with re-precipitation of fine particles [27].

Microstructural features, as observed in optical microscopy are described in Fig. 10. Change in grain orientation begins in the transition between TMAZ/stir zones. Here (see Fig. 10(a)), the grains are rotated by tool action and by reaching approximately 90^{o} tilting, some degree of recrystallisation takes place [25], represented by the substantial decrease in grain size. In the stir zone, recrystallisation is fully developed within the lamellae pattern, evidenced by a very fine grain size, shown in Figs. 10(b), (c) and (d). The different lamellae are formed due to an essentially non-chemical

mixture of BM's. It can be seen from the SEM-EDS micrographs in Figs. 10(e) and (f) the presence of peaks of copper (bright regions of the picture) and peaks of Si (dark regions of the picture). This leads to the conclusion that dark lamella originates from AA2024-T351 (Al-Cu alloy) and the bright lamella from AA6056-T4 (Al-Si-Mg alloys). Local microhardness measurements have also proved the origin of this lamellae pattern formation, where dark lamellae showed higher values of microhardness than bright lamellae, as confirmed in Fig. 10(b).

Fig. 11(a) shows the longitudinal section of the welded joint. As it can be seen the lamellae is oriented towards the welding direction. The observed pattern is a result of differential flow behaviour of each material and is assumed to be associated with the thread spacing used in the pin. The spacing between each lamella and their size is related to the employed weld pitch (tool rotation divided by the welding speed). Fig. 11(b) presents the lamellae with higher magnification. Here recrystallised grains can be observed. Fig. 11(c) presents the microhardness profile obtained perpendicular to the welding direction. In this case, values oscillate suggesting a lack of mixing of both alloys within the stir zone. As expected, low values are associated with bright lamellae (AA6056) and high values with dark lamellae (AA2024).

The xz-section is presented in Fig. 11(d), where the lamellae are observed from the top. Moving towards the TMAZ/stir zone transition, the grains become flattened up to a certain point where recrystallisation initiates.

At this moment grains suffer a substantial reduction in size as showed in Fig. 11(e). The microhardness profile for this section is presented in Fig. 11(f).

The region of the joint where thermocouple measurements were obtained has been sectioned to study local microstructure and microhardness (Fig. 12(a)). From the polishing sequences, the location of thermocouple 15 (nearest one to the AA6056) and 28 (third nearest to the AA2024 side) were localized. In this way the actual position of the remaining thermocouples could be determined. Figs. 12(b) and (c) show the microstructure where the thermal cycle from thermocouple 15 was recorded (on 6056-T4 side). Figs. 13(a) and (b) show the microstructure on the location of thermocouple 28. In both cases the microstructure, as observed by optical microscopy, appears identical to the respective base materials. Also the particles analysed by EDS displayed the same composition as the respective BM's (see Fig 7). However, the local microhardness data (average of two indentations) showed instead a variation from base material values. Figs. 12(d) and 13(c) present microhardness results at the location where thermocouples were placed together with the maximum temperature reached at that position. These diagrams displayed the same behaviour as seen in Fig. 9(b). Considering that the temperatures used for artificial ageing on the alloys of 2XXX and 6XXX series are around 200 $^{\circ}$C [28], it seems reasonable to assume that further precipitation took place until overaging mechanisms started to rule, explaining therefore the local increase in hardness between the HAZ and TMAZ in both alloys.

3.5. Mechanical Properties

Flat tensile specimens were produced parallel to the welding direction (specimens L-T). Table 3 shows the average joint efficiency in terms of tensile properties (yielding point, $Rp_{0,2\%}$, ultimate tensile strength, Rm, and elongation at rupture, ε_r) for 3 tested specimens, with reference to base material properties.

The joint efficiencies were calculated taking both base materials as reference. The stronger material (AA2024-T351) dictated the lowest strength undermatch because of its higher strength. Localised plasticity (stress concentration) on the TMAZ of the AA6056 led to failure. This phenomenon took place due to the large strength mismatch between both BM's. This is in accordance with the results of the cross section microhardness profiles (Figure 9(a)), which exhibit the lowest microhardness values in this region.

Microflat tensile test specimens were used to determine local properties through the welded joint. Figure 14 presents the results in terms of $\mathbf{Rp_{0,2\%}}$, Rm, and ε. The observed behaviour of the local tensile properties is in accordance with the microhardness results, showing a decrease in strength towards the weld centre on both sides of the joint. The elongation at rupture for the microflat tensile specimens in Figure 14 was obtained without the influence of stress concentration in the weld region, displaying values from 10% to 19%. These results are quite important as a tool for thermo-mechanical simulation studies since it provides a better understanding of local deformation.

4. Conclusions

Defect-free friction stir welds have been produced for the dissimilar alloys system AA2024-T351/AA6056-T4. From the thermal cycle measurements, maximum temperatures close to the weld centre measured during process were within 300-400^{o}C. Moreover, the temperature measurement techniques used (thermocouples and IR-camera) have supported the interpretations of microstructural aspects. No or very limited chemical mixing of the BM's in the stir zone could be observed with the experimental techniques used in this investigation. Only an intimate physical contact between BMs was observed. Tensile tests have shown reasonable joint efficiencies in terms of ultimate tensile strength (around 56.0% of the 2024-T351 and 90% of the 6056-T4 alloys) but poor efficiency in terms of elongation at the rupture (9.0%). This can be explained in terms of the stress concentration caused by the large difference in strength between BM's, leading to confined plasticity and then, to failure. The TMAZ of AA6056-T4 (weakest region within weld seam) was the location where a crack could initiate and propagate. Microflat tensile tests provided valuable data, which is representative of the local tensile properties for the joint and confirmed the general trend observed in he microhardness test results.

This study has shown that in a dissimilar friction stir weld, the weaker component dictates the performance of the joint, where failure happens in the

region of the greatest strength reduction related to annealing phenomena. Microscopic investigation as well as the evaluation of local mechanical properties has suggested that mechanical mixing is the major material flow mechanism in the formation of the stirred zone.

References

[1] W. Thomas, et al., Improvements relating to friction welding, international patent application No. PCT/GB92/02203, U.K., 1993.

[2] K.E. Knipström, Friction stir welding process goes commercial, Welding Journal. 9 (1997) 55-57.

[3] R.S. Mishra, Z.Y. Mab, Friction Stir Welding and Processing, Materials Science and Engineering. R50 (2005) 1-78.

[4] Welding Handbook Vol.3, American Welding Society, USA, 1996.

[5] R. Zettler, et al., Effect of tool geometry and process parameters on material flow in fsw of an AA 2024.t351 alloy, Welding in the World. 49 (3/4) 41-46, 2005.

[6] S. Benavides, et al., Low temperature friction stir welding of 2024 aluminum. Scripta Materialia. 41 (8) 809-815, 1999.

[7] Ch. Blanc, Y. Roques, G. Mankowski, Applications of phase shifting interferometric microscopy to studies of the behaviour of coarse intermetallic particles in 6056 aluminium alloy. Corrosion Science, 40 (6) 1019-1035, 1998.

[8] Http://www.pechiney.com, 6056-T4511/T6511/T8511 Weldable alloy- thin extrusions, a choice of high strength - corrosion resistant temper, Pechiney Aerospace. 12th Oct. 2001.

[9] R. Dif, et al., Recent development in aluminium sheets alloys used in aerospace. Pechiney Aerospace (internal publication), 2001.

[10] C. Wolwerton, Crystal structure and stability of complex precipitate phases in Al-Cu-Mg-(Si) and Al-Zn-Mg alloys, Acta Materialia. 49 (2001) 3129-3142.

[11] D.J. Chakrabarti, B.-K. Cheong, D.E. Laughlin, Precipitation in Al-Mg-Si-Cu alloys and the role of the Q-phase and its precursors, http://neon.mems.cmu.edu/laughlin/paper8/p8-1.html, 11th Dec. 2001.

[12] M.H. Jacobs, Precipitation hardening, in Training in Aluminium Application Technologies, European Aluminium Association. 2001.

[13] L.E. Murr, et al., A comparative study of friction-stir welding of aluminium alloys. Aluminium Transactions. 1 (1) 141-154, 1999.

[14] L.E. Murr, et al., Intercalation vortices and related microstructural features in the friction-stir welding of dissimilar metals, Materials Research Innovations. 2 (1998) 150-153.

[15] L. Ying, Solid-state flow visualization in the Friction-Stir Welding of 2024 Al to 6061 Al, Scripta Materialia. 40 (9) 1041-1046, 1999.

[16] T. Luijendijk, Welding of dissimilar aluminium alloys, Journal of Materials Processing Technology. 103 (2000) 29-35.

[17] H. Larsson, L. Karlsson, Joining of dissimilar Al-alloys by friction stir welding, in proc.: 2nd International Symposium on Friction Stir Welding. Gothenburg, Sweden, 2000.

[18] A. von Strombeck, C. Schilling, J.F. dos Santos, Robotic Friction Stir Welding - Tool Technology and Applications, in proc.: 2nd International Symposium on Friction Stir Welding. Gothenburg, Sweden, 2000.

[19] J.F. dos Santos, Monitoring and Control of FSW Process Parameters, in proc.: QUALISTIR Seminar and Final Demonstration, Geesthacht, Germany, 2003.

[20] ASTM E384-992e1, Standard test method for microindentation hardness of material, ASTM International, 2005.

[21] EN 910 DIN: Bending testing of welds in metallic materials, Europäisches Komitee für Normung, 1996.

[22] EN DIN 895, Qualitätsicherung in der Schweißtechnik, Querzugversuch, Europäisches Komitee für Normung, 1995.

[23] M. Koçak, et al. Microtensile test technique for weldments. GKSS Forschungszentrum, Germany, 1998.

[24] R. Zettler, F. Potomati, J.F. dos Santos, N.G. Alcantara, Temperature evolution and mechanical properties of dissimilar friction stir weldments when joining aa2024 and AA7075 with an AA6056 alloy, Welding in the World. 50 (11/12) 107-116, 2006.

[25] J.R. Davis, Aluminum and aluminum alloys 3rd ed., ASM International, 1996.

[26] P. Threadgill, Friction stir welds in aluminium alloys - preliminary microstructural assessment, Industrial Report 513/2/97 of The Welding Institute – TWI, 1997.

[27] J.C. Yuh, Q. Xinhai, Heat transfer and thermomechanical analysis of friction stir joining of AA 6061-T6 plates. in proc.: 1st Symposium on Friction Stir Welding, Thousand Oaks, California, 1999.

[28] L.F. Mondolfo, Aluminum alloys: structure and properties, Butterworths, U.K., 1976.

Figure 1 - FSW tool used in this work.

Figure 2 - Tricept 805 Robot.

Figure 3 - Weld seam sections analysed by optical and scanning electron microscopy.

Figure 4 – Location and dimensions of microflat tensile specimens.

Figure 5 – (A) Infrared System with welded plates, clamping system and IR-camera. (b) Cromel-Alumel Thermocouples System; Upper caption: plates and fixed thermocouples before welding. Lower caption: features and positioning of the thermocouples in the as-welded condition.

Figure 6 – (A) Maximum temperatures versus distance to the weld centre for thermocouples on the retreating side. (b) Maximum temperatures versus distance to the weld centre for thermocouples on the advancing side.

Figure 7 (A) Base material AA2024-T351 (500x) Flick. (b) SEM-BSE image of (a) (800x). (c) Base material 6056-T4. (500x), Dix-Keller. (d) SEM-BSE image of (c).

Figure 8 – Photo-montage displaying the macrostructure of a dissimilar AA2024-T351/AA6056-T4 joint and the investigated sections.

Figure 9 – (A) Cross section of produced weld seam. (b) Microhardness profiles from (a).

Figure 10 – (A) transition area between TMAZ/stir zones from Figure 9(a). (b) Higher magnification of Figure 9(a) in the position marked with a cross “X” in the nugget area. Notice

contrast among dark and bright lamellae. (c) Dark lamella, (1000x) in (b). (d) Bright lamella, (1000x) in (b). (e) SEM-BSE image of the stir zone, (45x). (f) SEM-BSE, stir zone, (150x). Lamellae colour in BSE image is reversed (i.e. dark lamella is bright and vice-versa) due to atomic number contrast mechanism.

Figure 11 – (A) Longitudinal section of the weld seam. (b) Details from the bottom area of (a) showing lamellae. (c) Microhardness profile of longitudinal section. (d) xz-section of the weld seam. (e) Magnified pictures from regions xx (left) and x (right) in (d). (f) Microhardness profile of the xz-section.

Figure 12 – (A) Schematic picture overlaying cross section and thermocouples locations across the weld. (b) Thermocouple 15, retreating side (AA6056) with the two local indentations used to determine the average microhardness. (c) SEM-BSE image of the particles present in (b). (d) Microhardness values for thermocouples 10 to 15, average of two measurements at the bottom of each hole. The maximum temperatures are also given.

Figure 13 – (A) Thermocouple 28, advancing side (AA2024) with the two local indentations used to determine the average microhardness. (b) SEM-BSE image of the particle present in (a). (c) Microhardness curve for thermocouples 24 to 30, average of two microhardness measurements at the bottom of each hole. The maximum temperatures are also given.

Figure 14 – Microflat tensile results of the produced weld. Each point on the curves represents the results of one microflat specimen.

Acknowledgements

The authors would like to acknowledge the financial support provided by the European Commission within the scope of the European Project WAFS. Research support for S.T. Amancio-Filho was provided by Conselho Nacional de Pesquisa CNPq – Brazil.

Figure1

Click here to download high resolution image

Figure2

Click here to download high resolution image

Figure3

Click here to download high resolution image

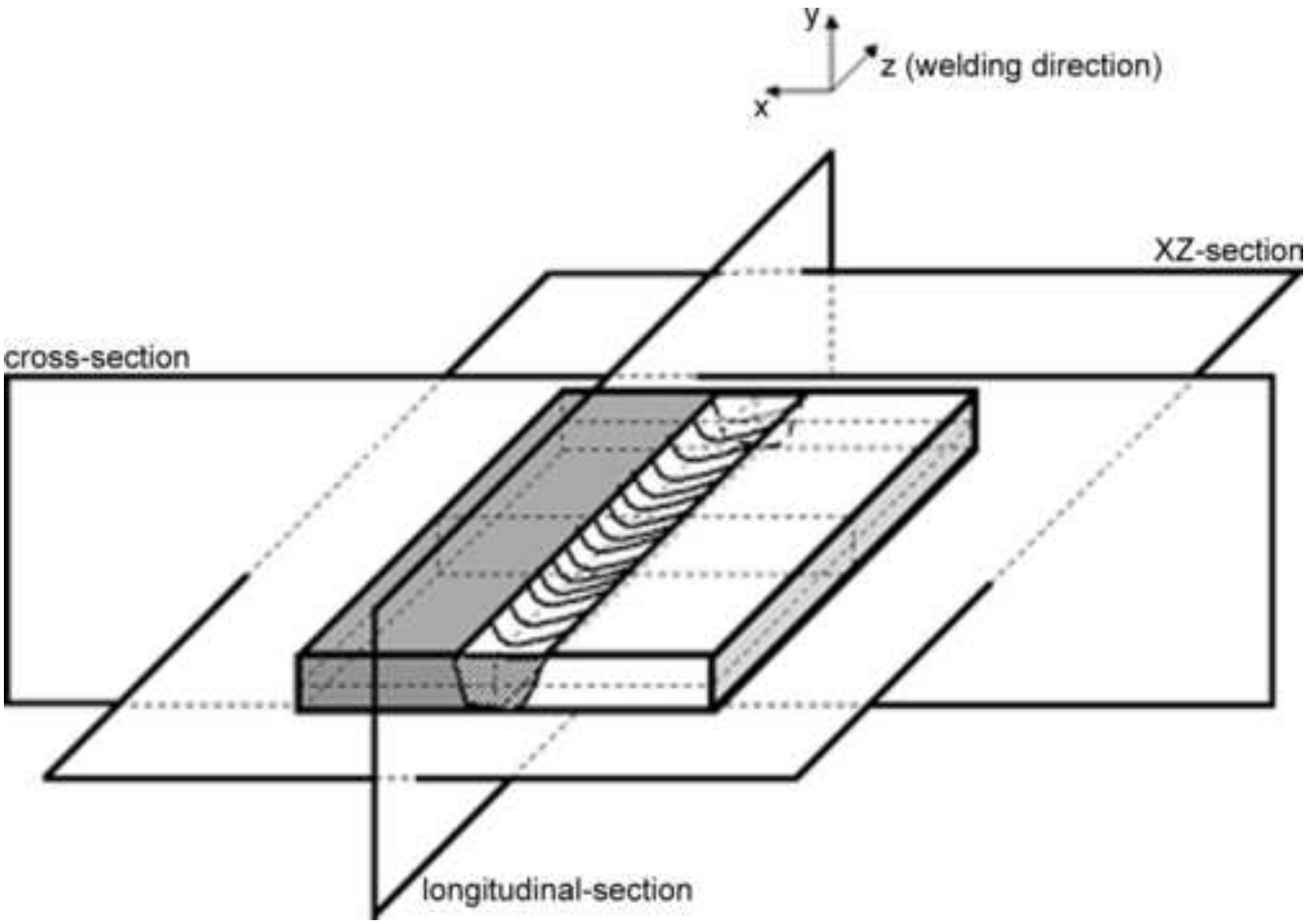

Figure4

Click here to download high resolution image

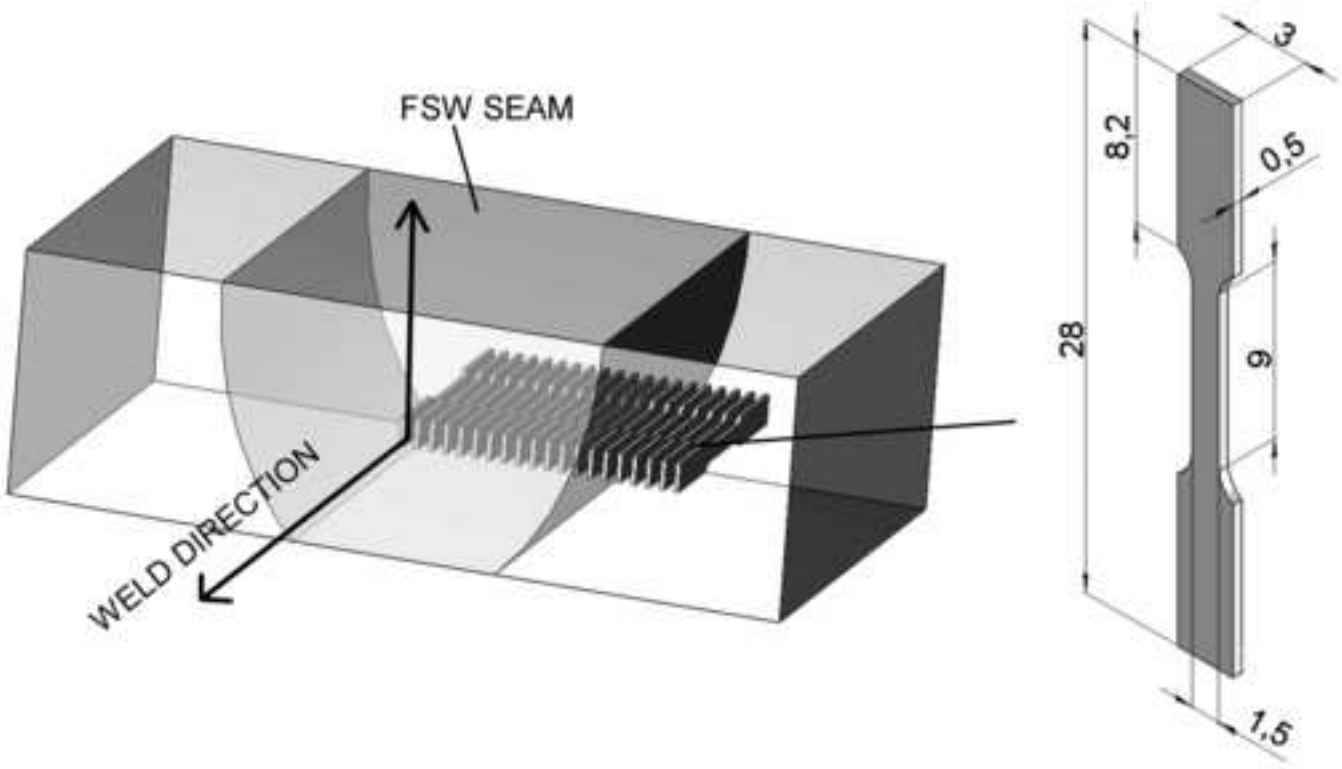

Figure5

Click here to download high resolution image

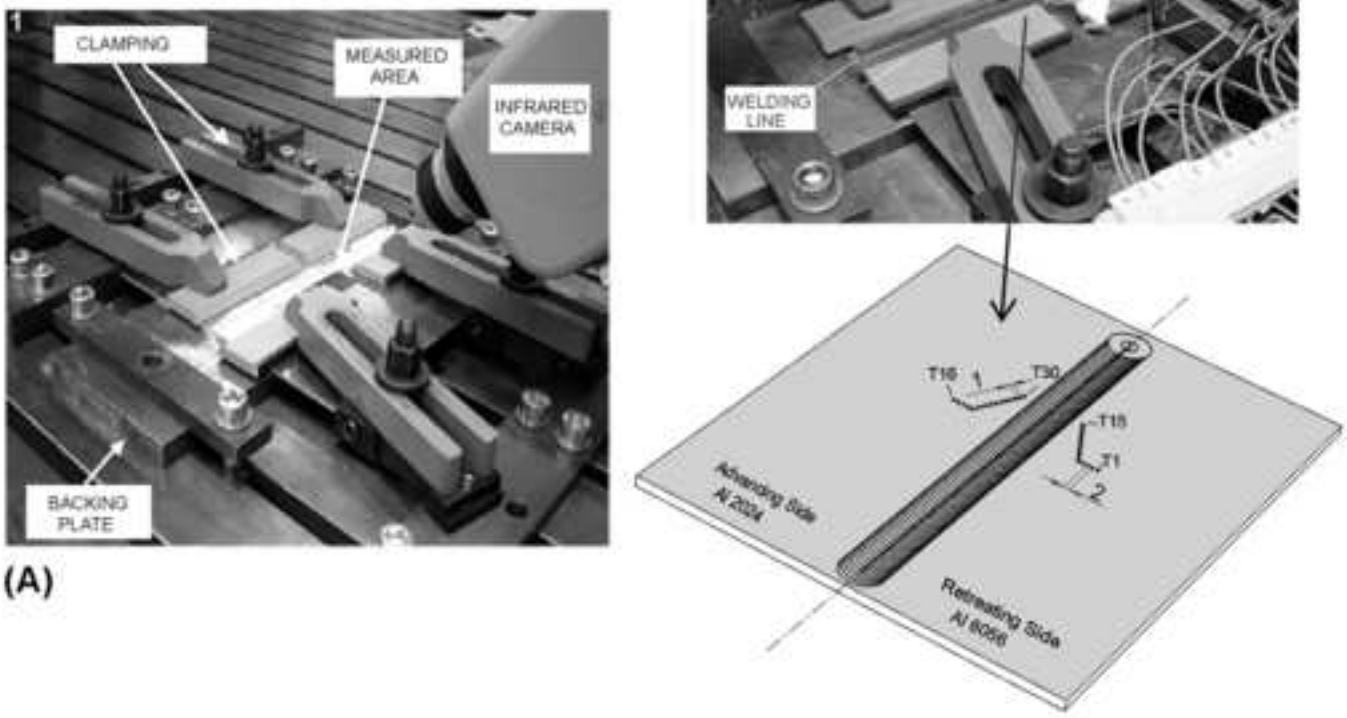

Figure6

Click here to download high resolution image

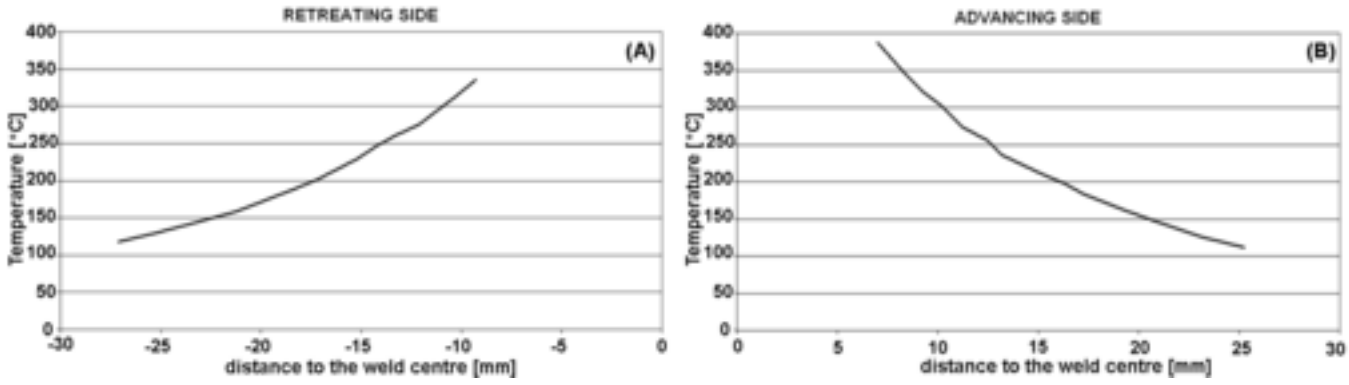

Figure7

Click here to download high resolution image

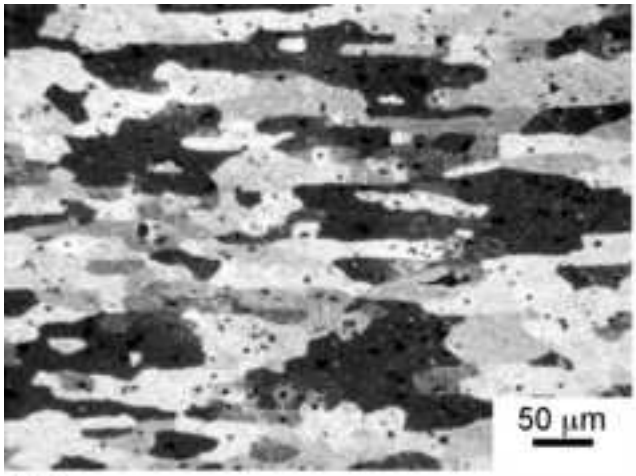

(A)

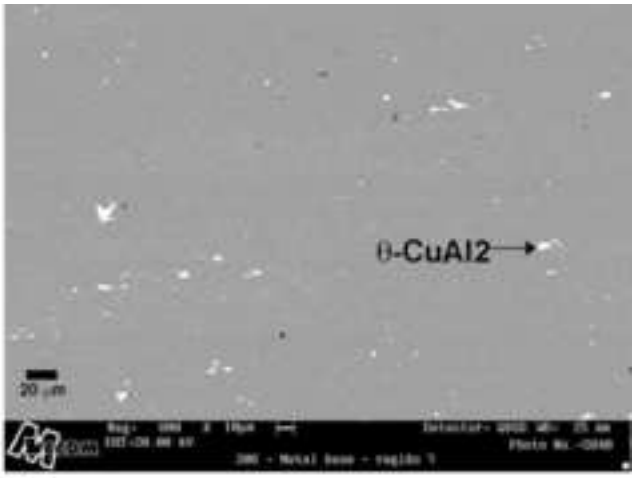

(B)

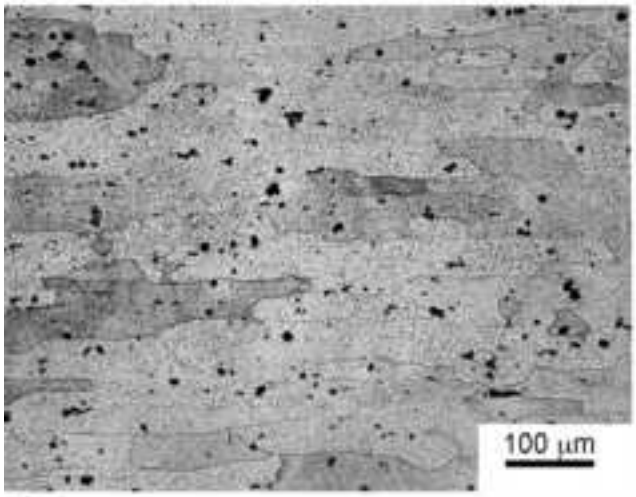

(C)

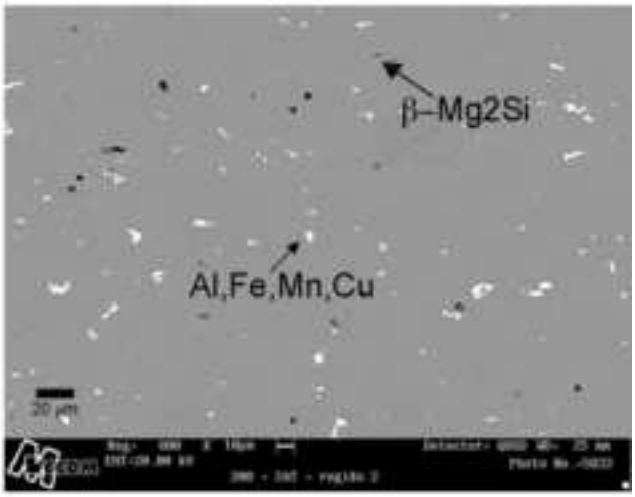

(D)

Figure8

Click here to download high resolution image

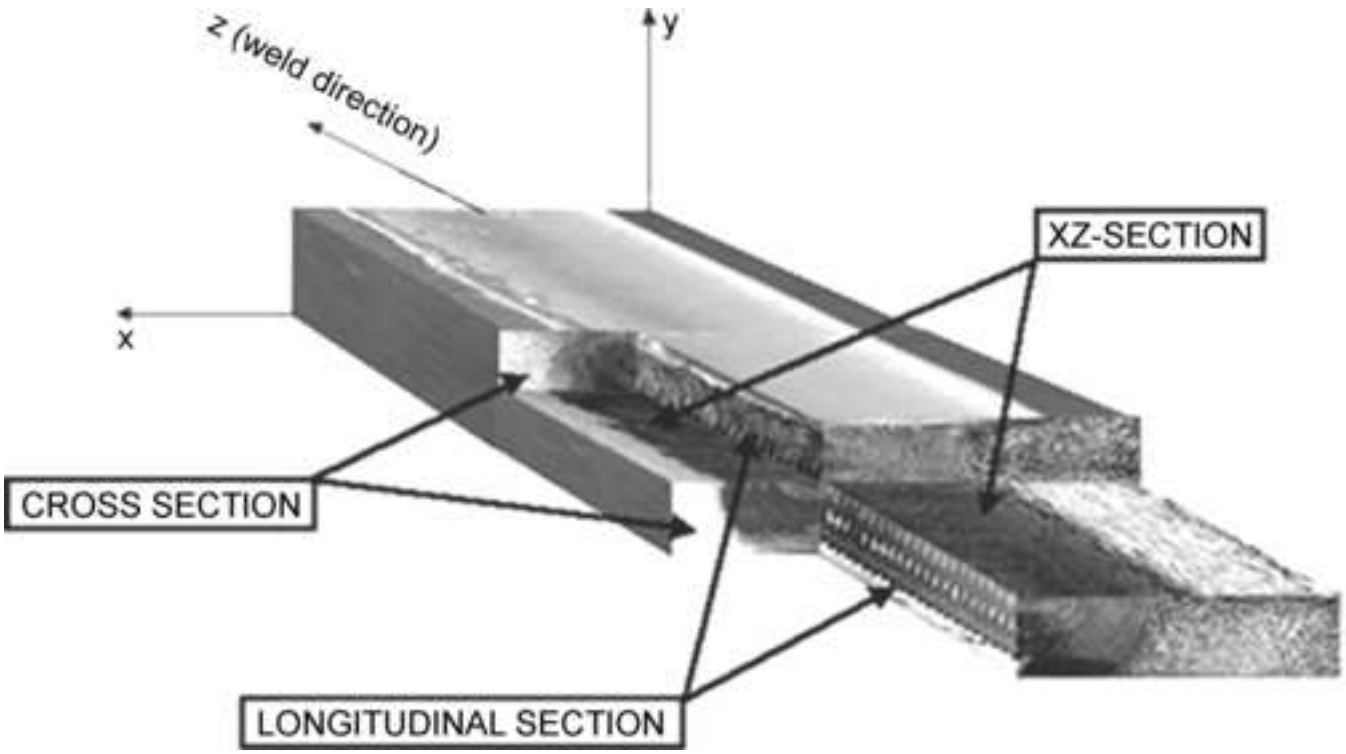

Figure9
Click here to download high resolution image

(A)

2 mm

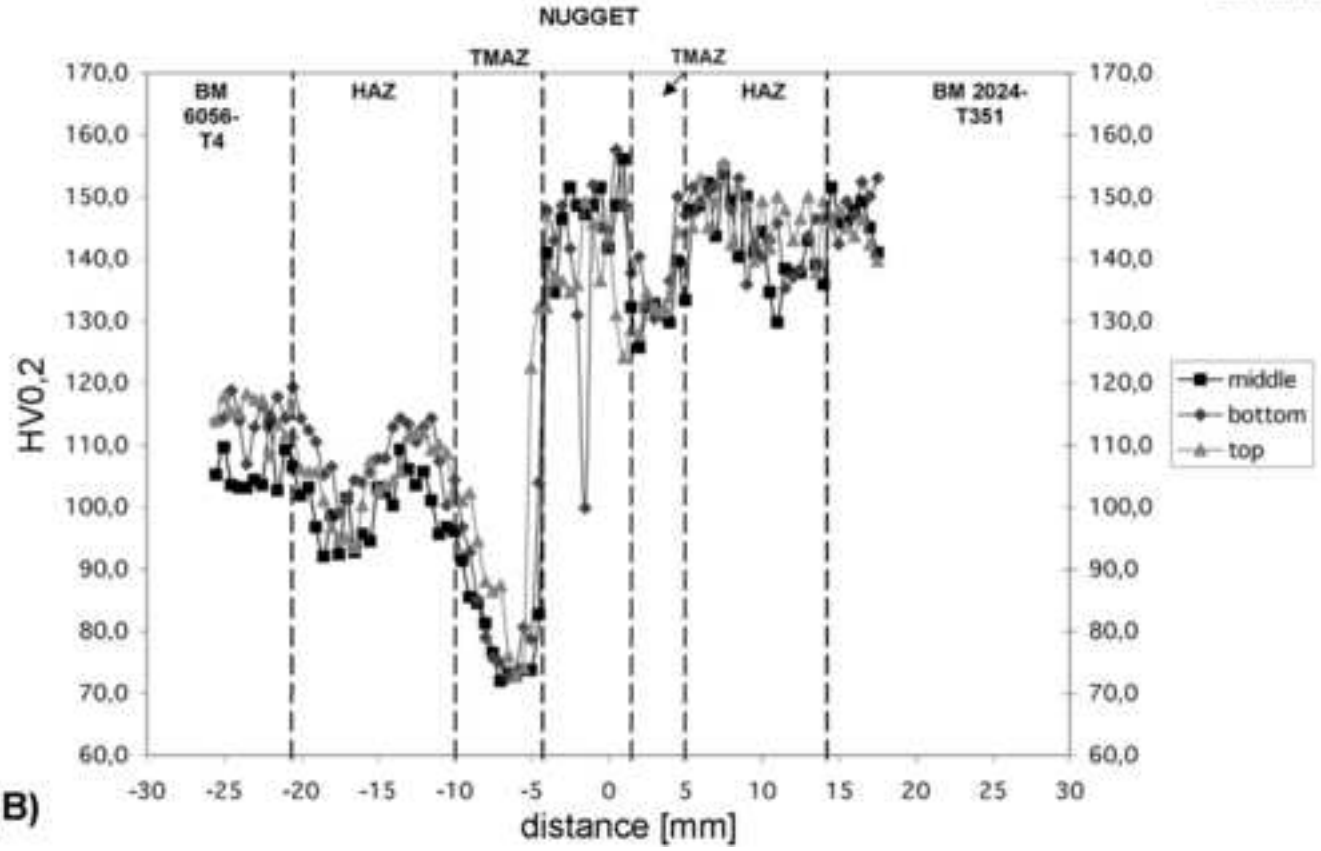

(B)

Figure10
Click here to download high resolution image

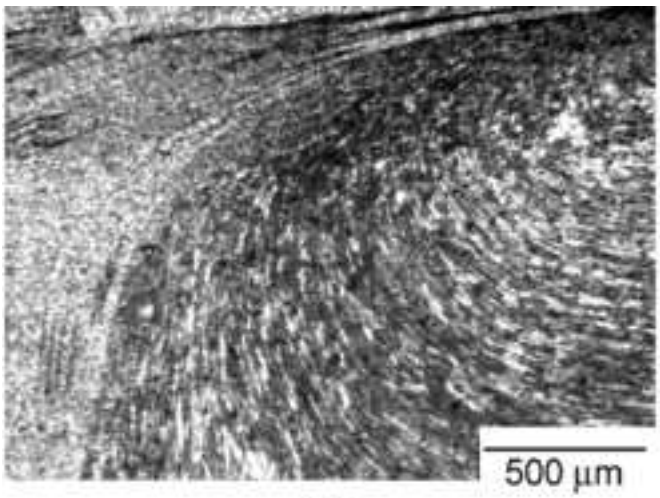

(A)

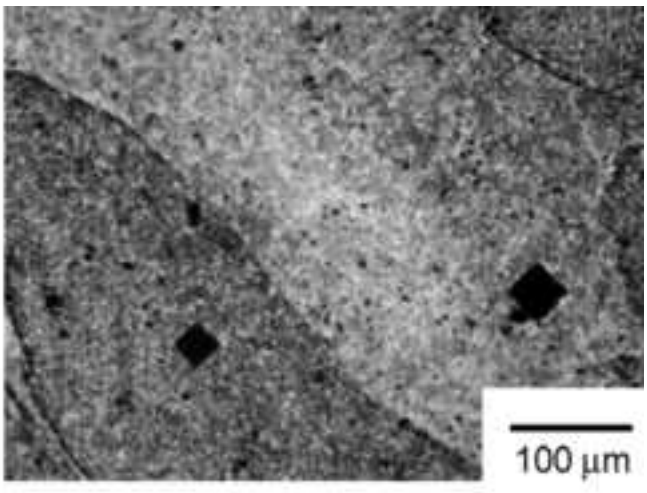

(B)

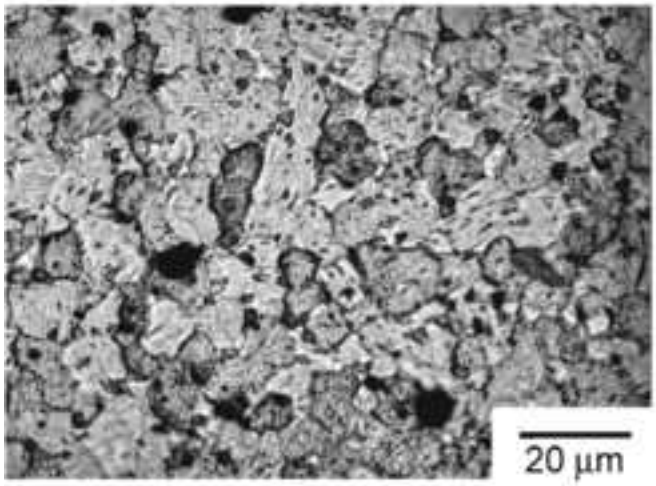

(C)

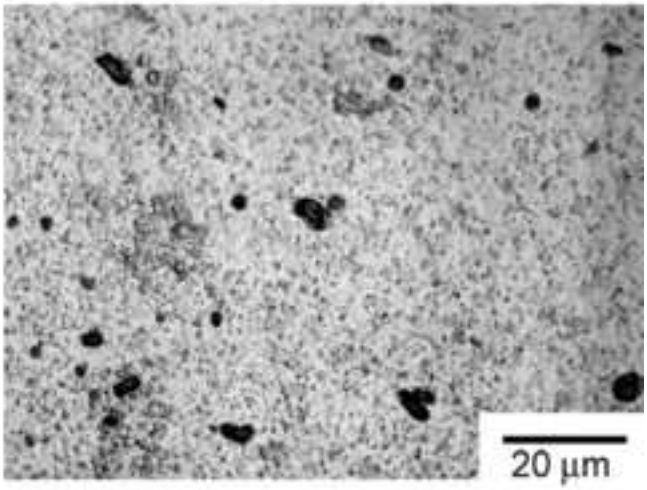

(D)

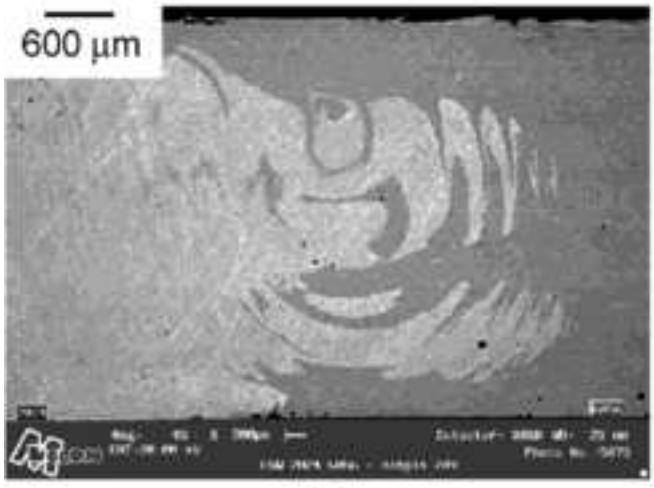

(E)

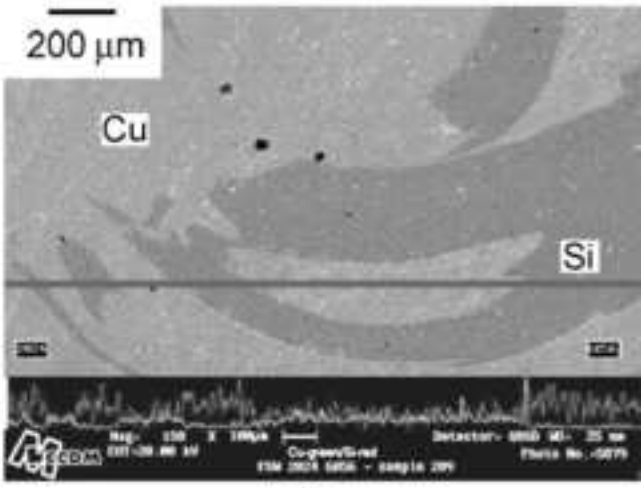

(F)

Figure11

Click here to download high resolution image

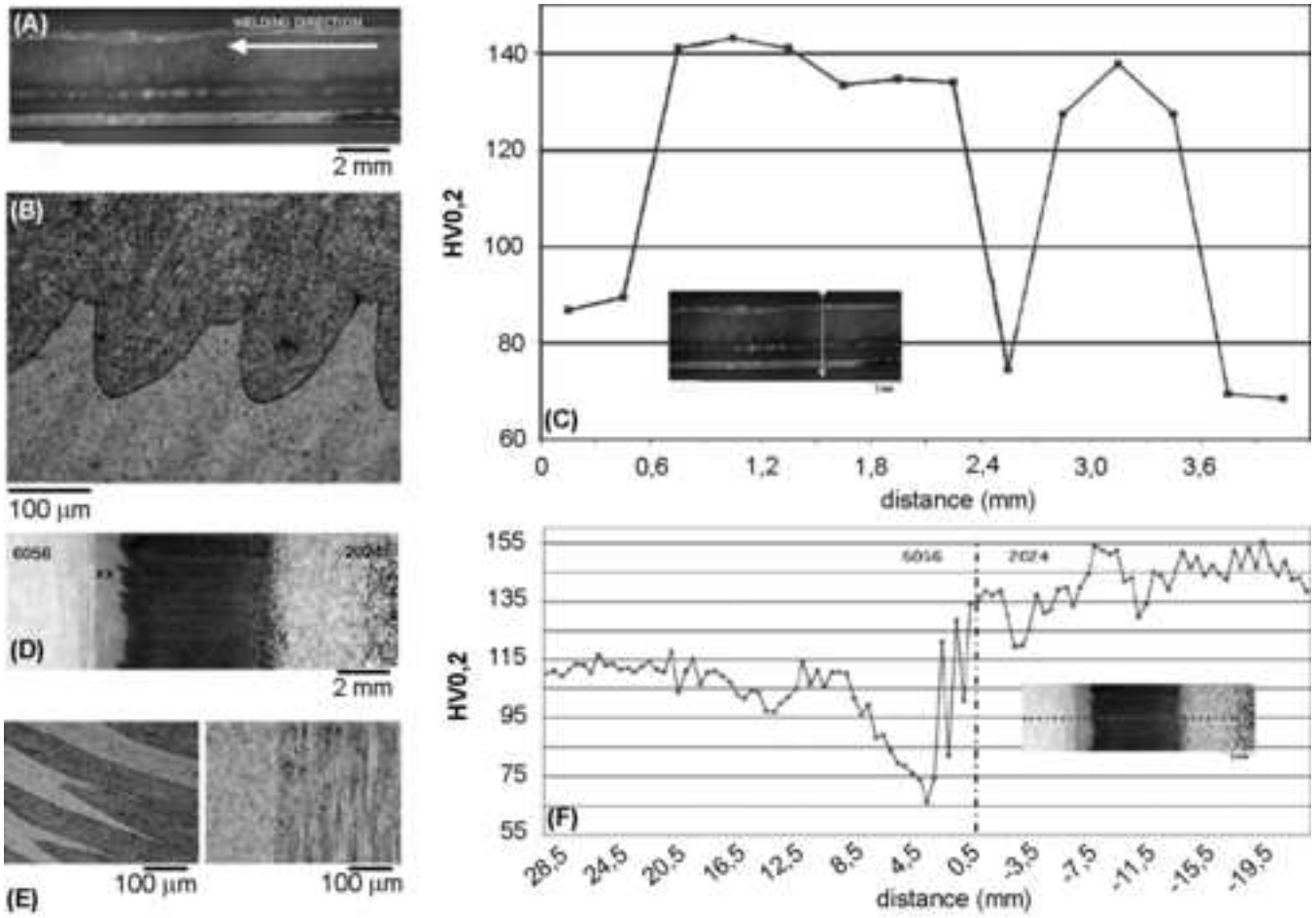

Figure12
Click here to download high resolution image

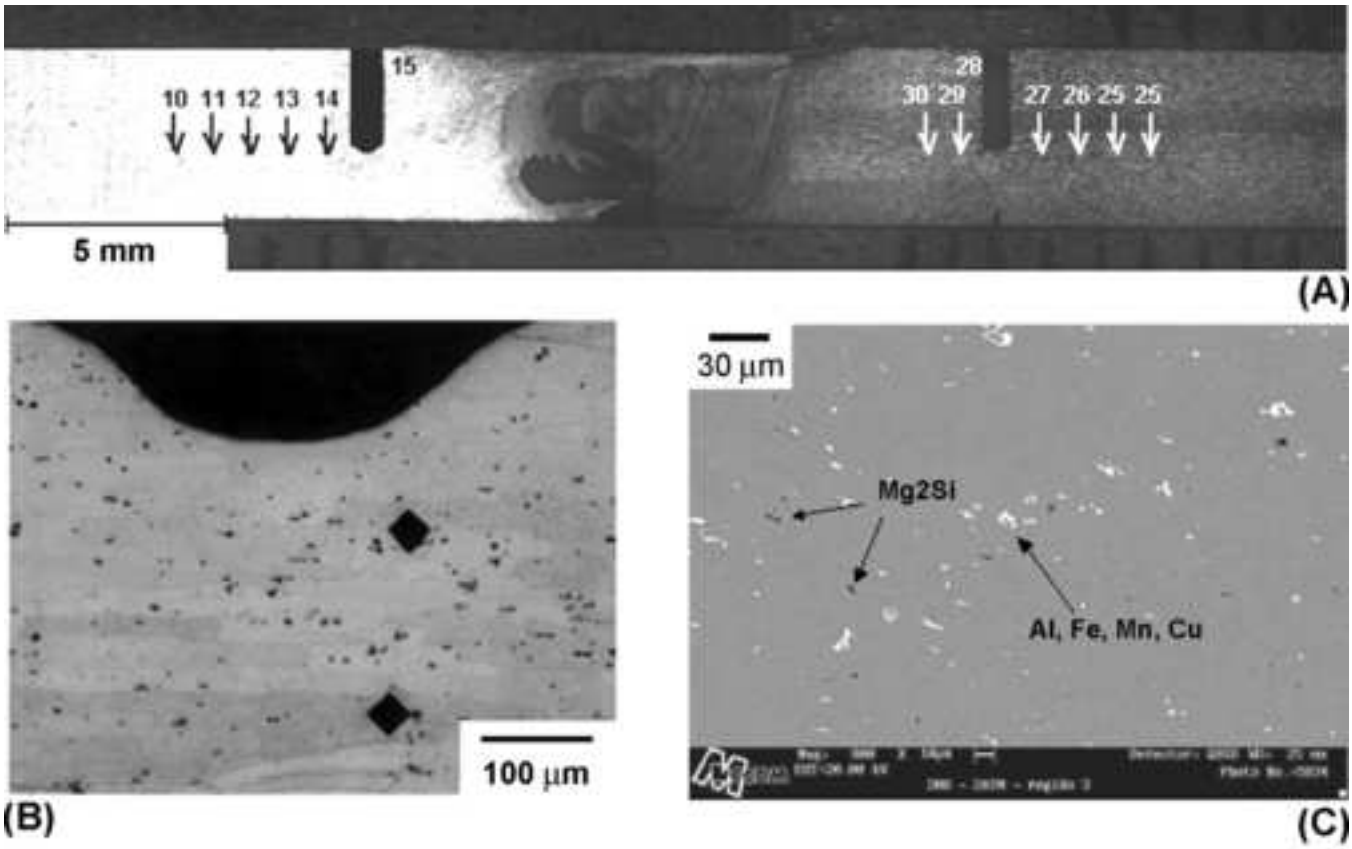

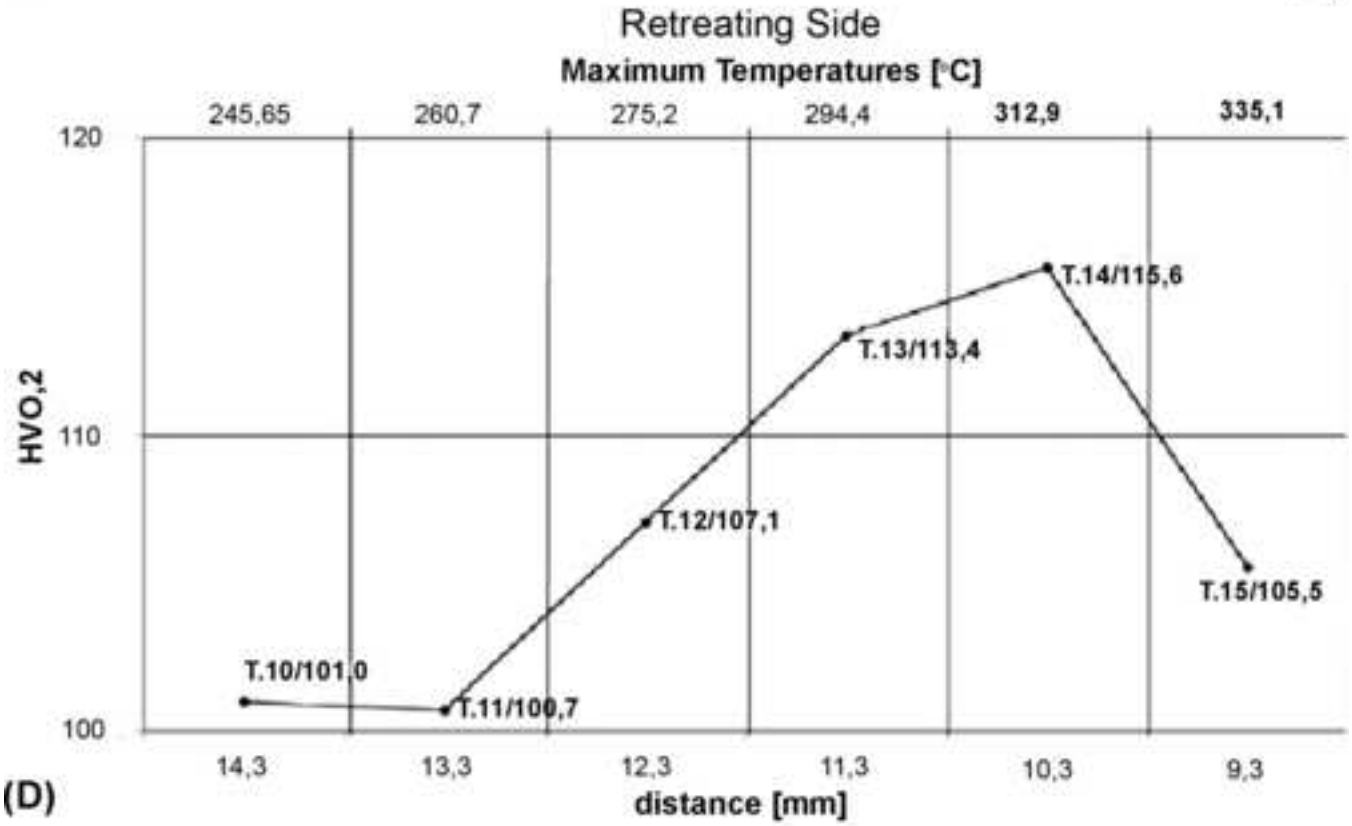

Figure13

Click here to download high resolution image

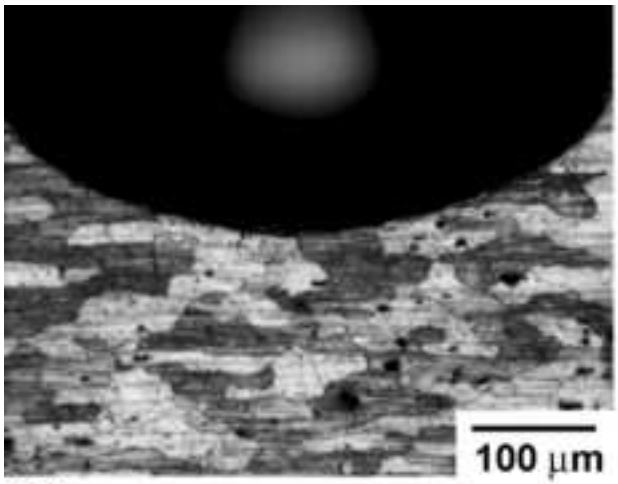

(A)

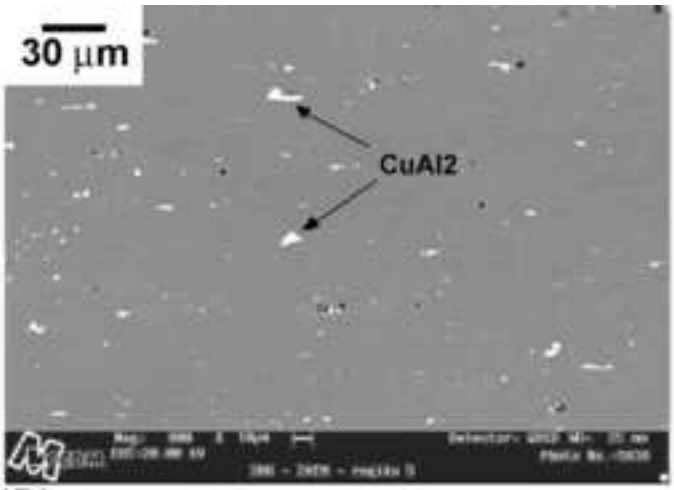

(B)

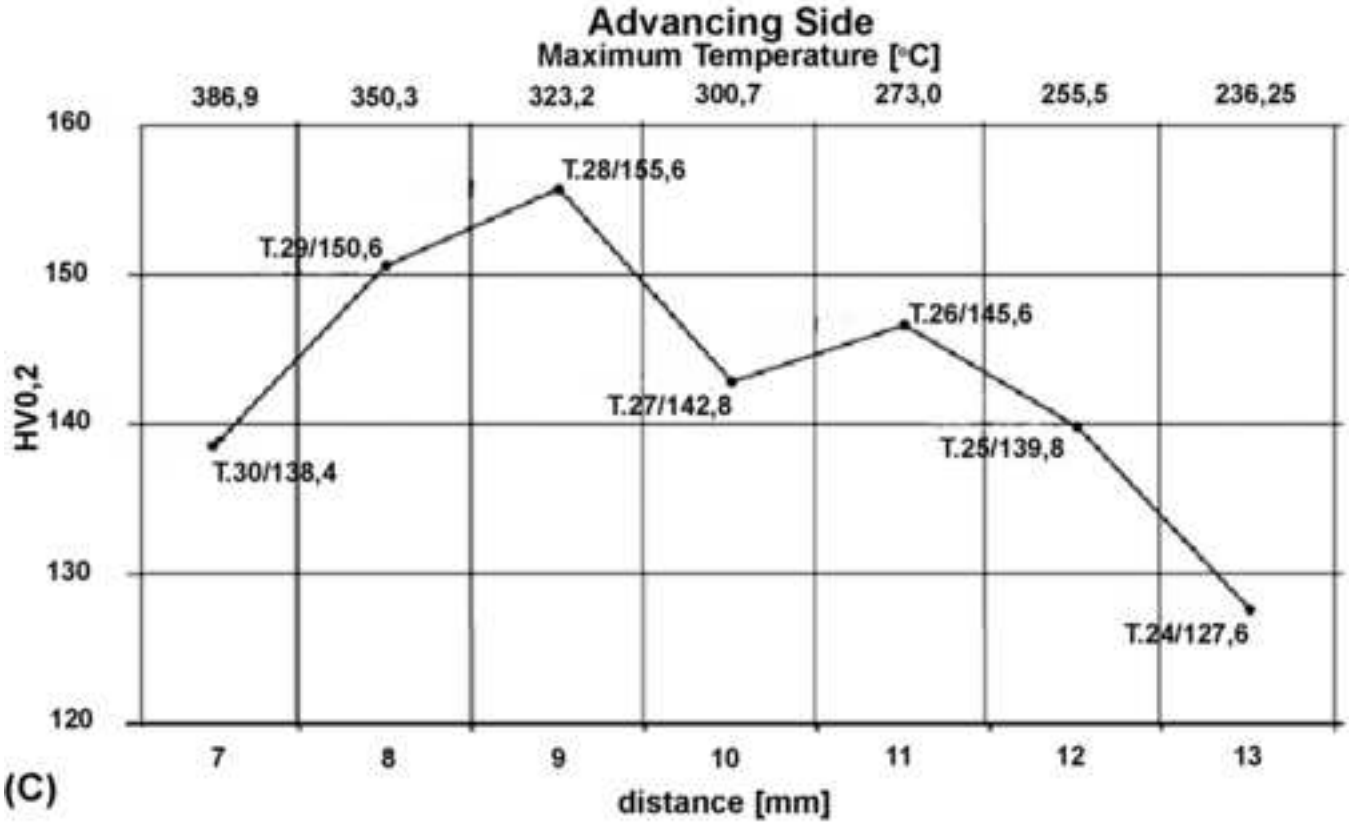

(C)

Figure14

Click here to download high resolution image

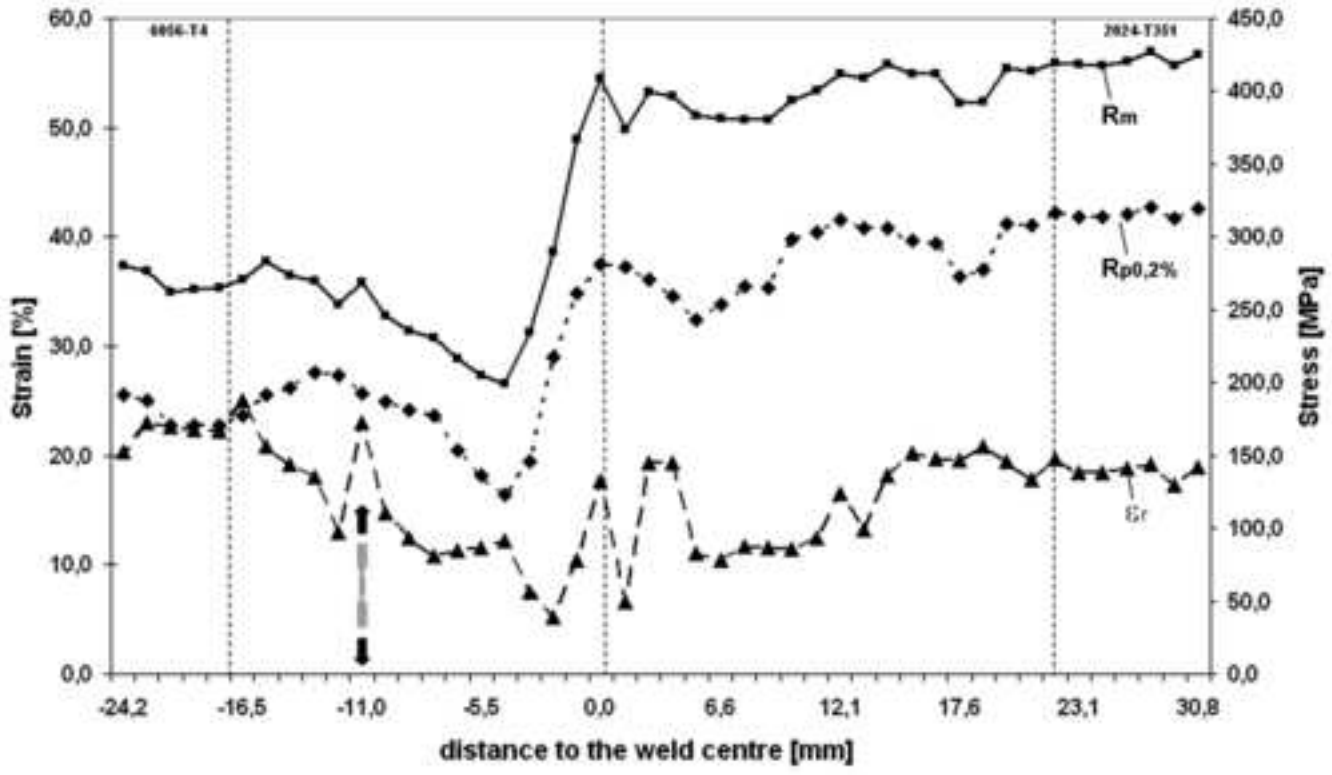

Table1

Click here to download high resolution image

Weight	Cu	Mg	Zn	Si	Fe	Al
(%)	3.870	1.340	0.086	0,0250	0,092	balanced

Table2

Click here to download high resolution image

Weight	Cu	Mg	Zn	Si	Fe	Mn	Al
(%)	0.700	0.710	0.190	1.2	0.180	0,660	balanced

Table3

Click here to download high resolution image

Base Mat.	$Rp_{0,2\%}$ (MPa)	Rm (MPa)	ε_r (%)	Joint Efficiency in terms of $Rp_{0,2\%}$ (%)		Joint Efficiency in terms of Rm (%)		Joint Efficiency in terms of ε_f (%)	
				2024	6056	2024	6056	2024	6056
2024-T351	290	440	14	-	-	-	-	-	-
6056-T4	224	344	21	-	-	-	-	-	-
Joint	201	246	1,9	69,3	89,7	55,8	71,4	9,0	14,0